International Journal of Minerals, Metallurgy and Materials
Volume 27, Number 3, March 2020, Page 328
https://doi.org/10.1007/s12613-019-1945-z

Evolution of plasticized $MnO–Al_2O_3–SiO_2$-based nonmetallic inclusion in 18wt%Cr–8wt%Ni stainless steel and its properties during soaking process

Jing Guo[1)], *Xing-run Chen*[2,3)], *Shao-wei Han*[4)], *Yan Yan*[1)], *and Han-jie Guo*[1)]

1) School of Metallurgical and Ecological Engineering, University of Science and Technology Beijing, Beijing 100083, China
2) State Key Laboratory of Advanced Metallurgy, University of Science and Technology Beijing, Beijing 100083, China
3) Jiuquan Iron and Steel Group Corporation, Jiayuguan 735100, China
4) Beijing Shougang Co. Ltd., Qian'an 064400, China
(Received: 17 October 2019; revised: 5 December 2019; accepted: 11 December 2019)

Abstract: The properties of $MnO–Al_2O_3–SiO_2$-based plasticized inclusion are likely to change during soaking process due to its low melting point. In this study, the evolution of the $MnO–Al_2O_3–SiO_2$-based inclusion of 18wt%Cr–8wt%Ni stainless steel under isothermal soaking process at 1250°C for different times was investigated by laboratory-scale experiments and thermodynamic analysis. The results showed that the inclusion population density increased at the first stage and then decreased while their average size first decreased and then increased. In addition, almost no Cr_2O_3-concentrated regions existed within the inclusion before soaking, but more and more Cr_2O_3 precipitates were formed during soaking. Furthermore, the plasticity of the inclusion deteriorated due to a decrease in the amount of liquid phase and an increase in the high-melting-point-phase $MnO–Cr_2O_3$ spinel after the soaking process. *In-situ* observations by high-temperature confocal laser scanning microscopy (CLSM) confirmed that liquid phases were produced in the inclusions and the inclusions grew rather quickly during the soaking process. Both the experimental results and thermodynamic analysis conclude that there are three routes for inclusion evolution during the soaking process. In particular, Ostwald ripening plays an important role in the inclusion evolution, i.e., $MnO–Al_2O_3–SiO_2$-based inclusions grow by absorbing the newly precipitated smaller-size $MnO–Cr_2O_3$ inclusions.

Keywords: nonmetallic inclusion; soaking process; Ostwald ripening; stainless steel

1. Introduction

Ultra-thin stainless steel strips are increasingly applied in many fields, such as home applications, instruments manufacture, and the automobile industry due to their outstanding complicated properties. Controlling a perfect surface quality for the ultra-thin stainless steel strip is difficult since nonmetallic inclusions have many opportunities to become exposed on the steel strip surface, which is one of the main causes for the generation of strip surface defects. Many researchers [1–10] found that the surface quality of stainless steel strip can be effectively improved by controlling the nonmetallic inclusion as low-melting-point $MnO–Al_2O_3–SiO_2$-based inclusion instead of $CaO–SiO_2–Al_2O_3$-based ones, and the $MnO–Al_2O_3–SiO_2$-based inclusion can be achieved by applying low-basicity refining slag and controlling low dissolved aluminium ([Al]s) content in steel during the smelting process.

Moreover, the $MnO–Al_2O_3–SiO_2$-based inclusion has a very low melting point that it can fully exist as the liquid phase or partly exist as the liquid phase at a soaking temperature between 1150 and 1250°C, indicating that this inclusion type is more likely to react with the steel matrix and evolve to other types of inclusion. In addition, stainless steels contain many alloy elements such as Cr and Ni; thus, an interaction can likely be induced between $MnO–Al_2O_3–SiO_2$-based inclusion and the steel matrix. Many researchers have noted that the nonmetallic inclusion would change in shape, size, and/or composition during heat treatment. Takano *et al.* [11] found in the 17Cr–9Ni stainless steel that a large num-

Corresponding author: Jing Guo E-mail: guojing@ustb.edu.cn

ber of $MnO–Cr_2O_3$ inclusions precipitated during heat treatment, and this kind of small-size inclusions could pin austenite grain boundaries. In particular, in a special issue on *ISIJ International* (2011, vol. 51, No.12), regarding "Fundamentals and applications of nonmetallic inclusions in solid steel", the behavior of inclusion in solid steel including stainless steel during heat treatment was intensively discussed. Shibata *et al*. [12–13] discovered that inclusions transferred from $MnO–SiO_2$ to $MnO–Cr_2O_3$ during heat treatment, and they analyzed the effects of Si, Mn, Ni, and Cr contents on the inclusion evolution. Taniguchi *et al*. [14] studied the inclusion change in martensitic stainless steel and proposed three routes for nonmetallic inclusion phase transformation during heat treatment. Ren *et al*. [15] also reported that $MnO-SiO_2$ type inclusion would transform to $MnO–Cr_2O_3$ spinel-type inclusion during the soaking process, and they proposed that the modification was due to Cr reducing the SiO_2 in $MnO–SiO_2$-based inclusion. Wang *et al*. [16] tried to illuminate its thermodynamic and kinetic mechanisms. In addition, other researchers [17–20] have noted that sulfide inclusion would also be transformational during the heat treatment process. However, to date, the behaviors of nonmetallic inclusion during heat treatment are still not fully understood; the thermodynamics of the chemical reactions and inclusion evolution mechanism are not very clear, and the present proposed mechanism does not well explain some phenomena such as the inclusion size change and composition evolution.

In the present study, steel samples containing mainly $MnO–Al_2O_3–SiO_2$-based inclusions were prepared, and they were subjected to isothermal soaking for different times at 1250°C to reveal the nonmetallic inclusion evolution process. Furthermore, high-temperature confocal laser scanning microscopy (CLSM) was also performed to deeply understand the behavior of the inclusion during the soaking process. Finally, a thermodynamic analysis was performed, and Ostwald ripening was introduced to explain the inclusion evolution mechanism.

2. Experimental

2.1. Materials

Steel specimens were taken from an industrial 18wt%Cr–8wt%Ni stainless steel continuous casting slab as mother alloy. They were machined firstly into the cubic samples with the size of 15 mm × 15 mm × 15 mm and were then used for laboratory-scale isothermal soaking experiments. To obtain the $MnO–Al_2O_3–SiO_2$-based inclusion, the industrial 18wt%Cr–8wt%Ni stainless steels (detailed composition as shown in Table 1) were smelted by a low-basicity refining slag (mass ratio of CaO/SiO_2 approximately 1.5). The composition of $MnO–Al_2O_3–SiO_2$-based inclusions was obtained by scanning electron microscopy/energy-dispersive spectroscopy (SEM/EDS, EVO 18/X-Max Extreme) before soaking treatment.

Table 1. Stainless steel composition in the present experiment wt%

C	Si	Mn	P	S	Cr	Ni	Al	T.O	Fe
0.054	0.408	1.190	0.033	0.001	18.170	8.040	0.0009	0.0035	Bal.

Note: T.O represents total oxygen in stainless steel samples.

2.2. Isothermal soaking experiments

The soaking experiments were carried out in a muffle furnace with four $MoSi_2$ electrodes. The whole experimental process was protected in an argon atmosphere with a rate of 200 mL/min. First, the temperature was raised to 1250°C at a heating rate of 10°C/min. Then, the temperature was held for 0, 30, 60, and 120 min, corresponding to steel samples marked as 1#, 2#, 3#, and 4#, respectively. After the soaking process, the samples were quenched in the water. The heating history of the soaking experiments was schematically shown as Fig. 1. The quenched steel samples were ground and mirror-polished for SEM/EDS observation. At the same time, an automated inclusion analyzer (EVO18, Zeiss, German) was applied to determine the inclusion morphology, size, and composition evolution during the soaking process, in which the area of 5 mm × 5 mm in each sample was detected in a stated path. Moreover, Cr element was usually de-

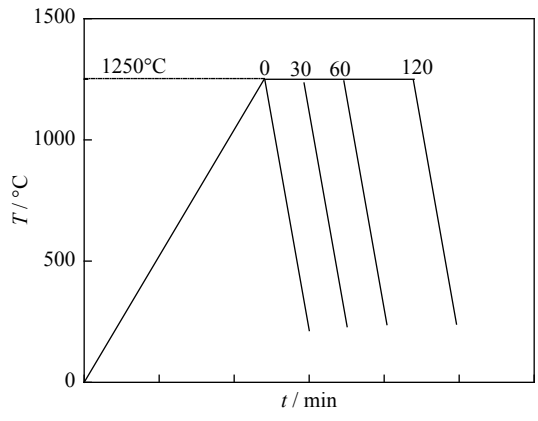

Fig. 1. Schematic of the heating process in soaking experiment.

tected in the inclusion by EDS, but it is not easy to confirm whether the Cr element was in the inclusion or not since the steel matrix contained 18wt% Cr. This issue should be considered by additionally using SEM-mapping and/or line scanning. In addition, some unclear spots detected were selected and excluded before the inclusion analysis.

2.3. *In-situ* observation by CLSM

To further clarify the nonmetallic inclusion evolution during soaking process, an *in-situ* observation method was applied using CLSM (VL2000DX-SVF17SP, LASERTEC Inc., Japan). The CLSM technique can achieve the real-time and continuous observation of the heating or cooling process on the steel sample surface at high temperatures. First, steel specimens were machined into a thin spherical wafer (7.5 mm in diameter and 2.5 mm in height), and then, they were ground and mirror-polished for further observation. The steel samples were heated from room temperature to 1250°C and held for 30 min to simulate the soaking process. Afterward, the samples were rapidly cooled to room temperature by introducing He gas (the cooling rate was about 300°C/min). Real-time videos of the entire inclusion transformation process were recorded and saved in a built-in system.

3. Results

3.1. Inclusion composition in steel before soaking process

Fig. 2 shows the inclusions composition in the 18wt%Cr–8wt%Ni slab projected in an isothermal $MnO–Al_2O_3–SiO_2$ ternary-phase diagram which is calculated by FactSage. Their main components were SiO_2, MnO, and Al_2O_3. The contents of other components, such as CaO, MgO, and TiO_2, were very small; hence, these components are not projected in the phase diagram. In addition, most of the inclusions were located in regions with melting point lower than 1300°C, indicating that the inclusions were well plasticized since they were likely to soften during the rolling temperature. In addition, most of the inclusions were smaller than 5 μm in size.

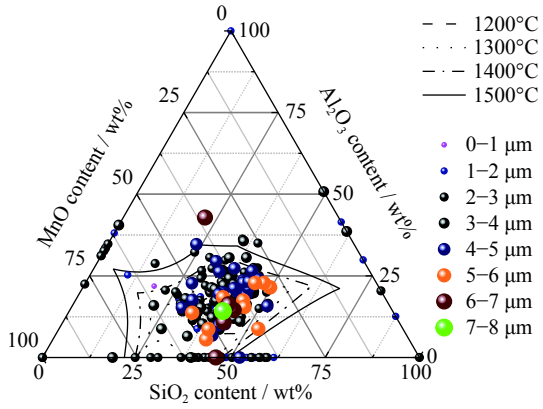

Fig. 2. Composition of nonmetallic inclusion of the slab matrix projected in isothermal $MnO–Al_2O_3–SiO_2$ ternary-phase diagram.

3.2. Morphology, composition, population density, and size evolution of inclusions during soaking process

Fig. 3 shows some typical individual inclusion morphologies observed from the examined steel samples and their main components. It should be pointed out that a small number of other components, such as CaO, MgO, and TiO_2 (lower than 10wt%), are not displayed in the figure. As shown in Fig. 3(a), the inclusion had an analogous spherical morphology, approximately 3 μm in size, and was composed of 44wt% SiO_2, 19wt% Al_2O_3, 22wt% MnO, 9wt% CaO, and 7wt% MgO, similar to the composition of the inclusion in the slab before soaking, as displayed in Fig. 2. No or very low Cr_2O_3 content was detected in most inclusions in the samples. Fig. 3(b) shows a typical inclusion in the steel sample after soaking for 30 min (sample 2#), in which many small-size Cr_2O_3–MnO-based inclusions with irregular morphologies were observed surrounding the primary inclusion that consists of $SiO_2–Al_2O_3–MnO–Cr_2O_3$. More Cr_2O_3 content was detected in the main inclusion, which is different from that in the slab or in sample 1#. As shown in Figs. 3(c) and 3(e), the Cr_2O_3 content in the inclusion matrix further increased after soaking for 60 and 120 min, and some Cr_2O_3-concentrated regions could be also detected. In addition, faceted $MnO–Cr_2O_3(–Al_2O_3)$-based inclusions were also detected. They were much smaller in size and became <1 μm and 1–2 μm after soaking for 60 min and 120 min, respectively, as depicted in Figs. 3(d) and 3(f).

Fig. 4 shows the evolution of the average inclusion composition during the soaking process. As the soaking proceeds, the average Cr_2O_3 content gradually increased while the SiO_2 content decreased. During 30 to 120 min of soaking (2#–4#), the MnO content in the inclusion remained almost the same. In addition, the CaO content also presented a slight decrease, and the TiO_2 content exhibited a small increase. The Al_2O_3 and MgO contents were fluctuant and their contents did not show significant change tendency during the soaking process.

Fig. 5 shows the inclusion population density and the evolution of average inclusion size during the soaking process. After soaking for 30 min, the inclusion population density increased as a large number of small-size Cr_2O_3–MnO-based inclusions precipitated during the soaking process so that the average inclusion size decreased cor-

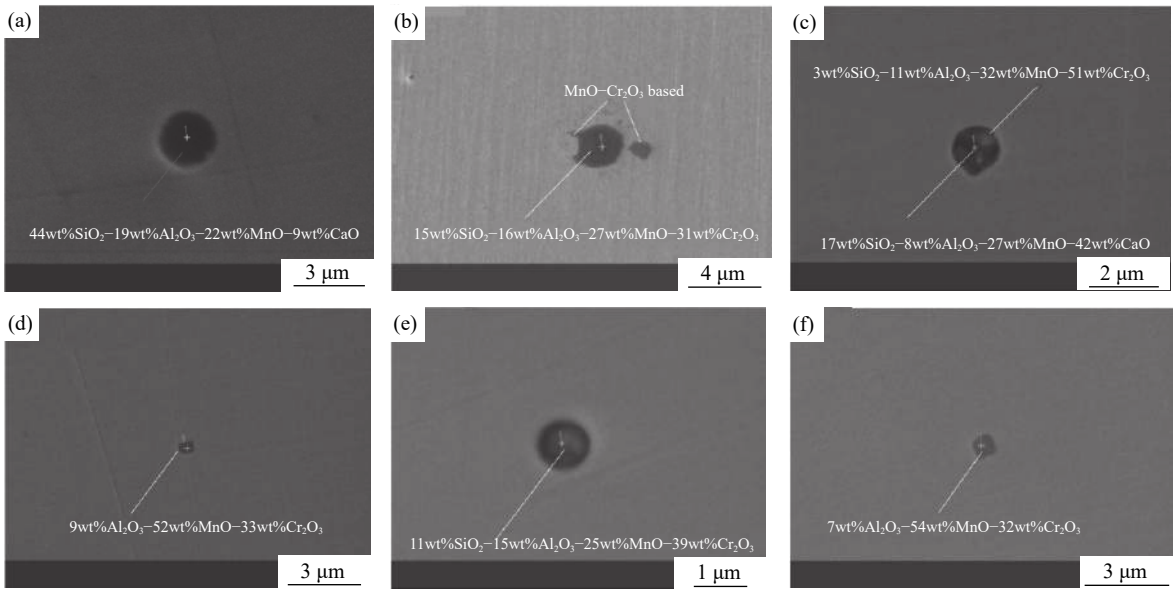

Fig. 3. Morphologies and compositions of some typical inclusions in different steel samples from the soaking process: (a) 1#; (b) 2#; (c, d) 3#; (e, f) 4#.

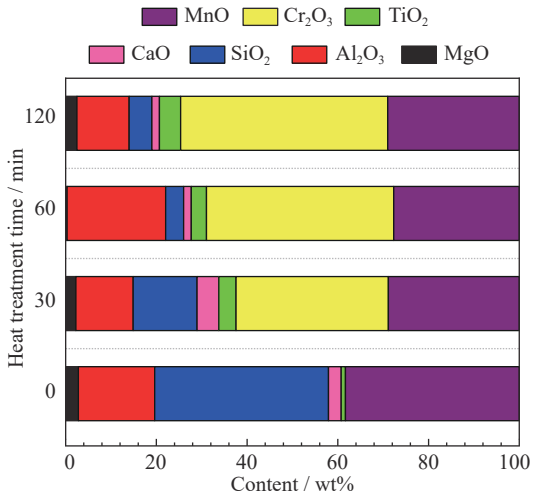

Fig. 4. Component evolution of nonmetallic inclusion during soaking process.

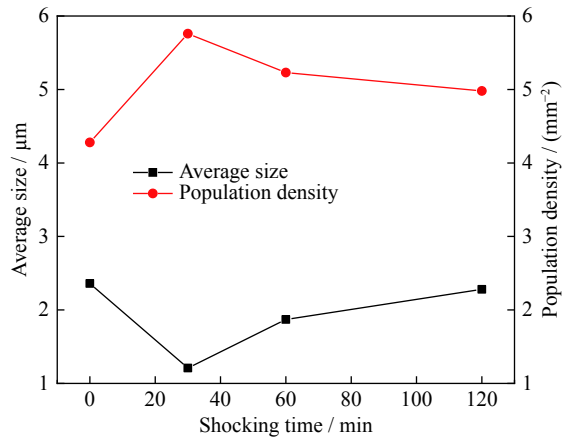

Fig. 5. Evolution of population density and average size of nonmetallic inclusion during soaking process.

respondingly. With the soaking time rise, the inclusion population density decreased and their average size increased gradually. Ren *et al.* [15] also observed similar inclusion number evolution and size distribution as those in Fig. 5. The inclusion growth followed the Ostwald ripening manner: the small inclusions dissolved, and the larger inclusions grew by absorbing the small ones.

3.3. Line scanning and SEM-mapping of inclusions during soaking process

Fig. 6 shows images of the line scanning results of Cr element in the two typical inclusions in steel samples 1# and 2# to further confirm the content of Cr-containing oxide at different stages of the soaking process. As shown in Fig. 6(a), no Cr-enriched part existed within the inclusion at the beginning of soaking, while Cr-containing oxide-enriched part was detected in the upper corner of the inclusion with lighter color after soaking for 30 min. This confirms that Cr_2O_3 is usually absent in the inclusion in an 18wt%Cr–8wt% Ni stainless steel slab before soaking and precipitates in the inclusion gradually during the soaking process. It should be pointed out Cr element is usually detected in the inclusions of stainless slabs by EDS due to the disturbances of the steel matrix composition.

Figs. 7–10 shows SEM-mapping images of some typical inclusions in the steel samples at different stages of the soaking process. From Fig. 7, Si, Ca, Mn, Al, and Mg elements were distributed almost homogenously and no Cr oxide-con-

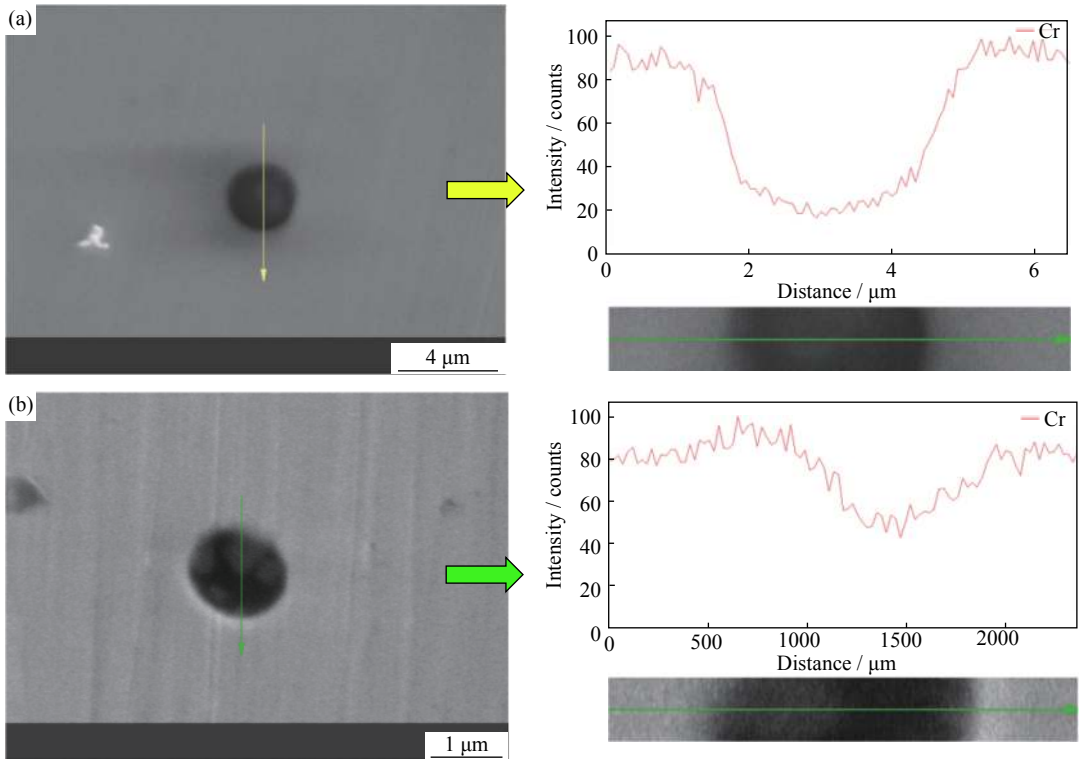

Fig. 6. Line scanning of Cr element in inclusions at different stages of soaking process: (a) 1#; (b) 2#.

centrated region existed within the whole inclusion, indicating the inclusion is a CaO–MgO–MnO–Al_2O_3–SiO_2 multi-component inclusion. As shown in Fig. 8, some blocky MnO–Cr_2O_3(–Al_2O_3)-concentrated regions were observed in the outer layer within the inclusion, and the other parts were CaO–SiO_2-enriched in composition after heat treatment for 30 min. As shown in Fig. 9, when the steel sample was soaked for 60 min, the inclusions mostly comprised MnO–Cr_2O_3-concentrated regions and only a small amount of CaO–SiO_2-concentrated region in the top-left corner. Interestingly, a ring-like CaO–SiO_2-concentrated region was detected in the inclusion after soaking for 120 min, as shown in Fig. 10, and a MnO–Cr_2O_3(–Al_2O_3)-enriched region was detected in the central part of the inclusion. Among the inclusions shown in Figs. 8–10, the MnO–Cr_2O_3-enriched region and the CaO–SiO_2-concentrated region seem incompatible and complementary.

3.4. *In-situ* observation of inclusion evolution during soaking process by CLSM

As shown in Fig. 11(a), only some small inclusion particles, marked by white arrows, were observed. With tem-

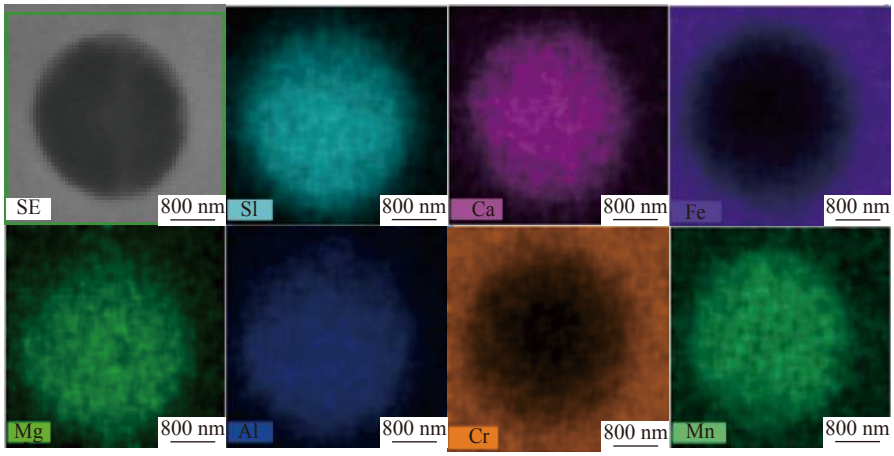

Fig. 7. SEM-mappings of typical inclusion in the steel after shocking for 0 min (1# sample).

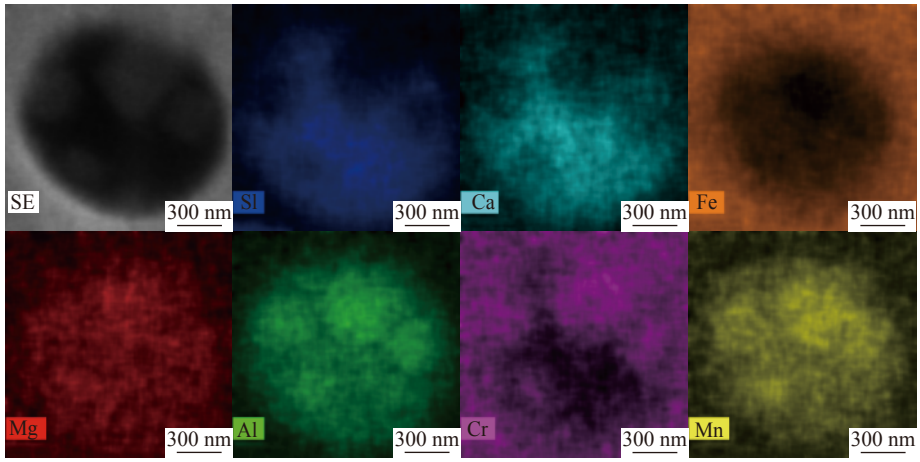

Fig. 8. SEM-mappings of typical inclusion in the steel after shocking for 30 min (2# sample).

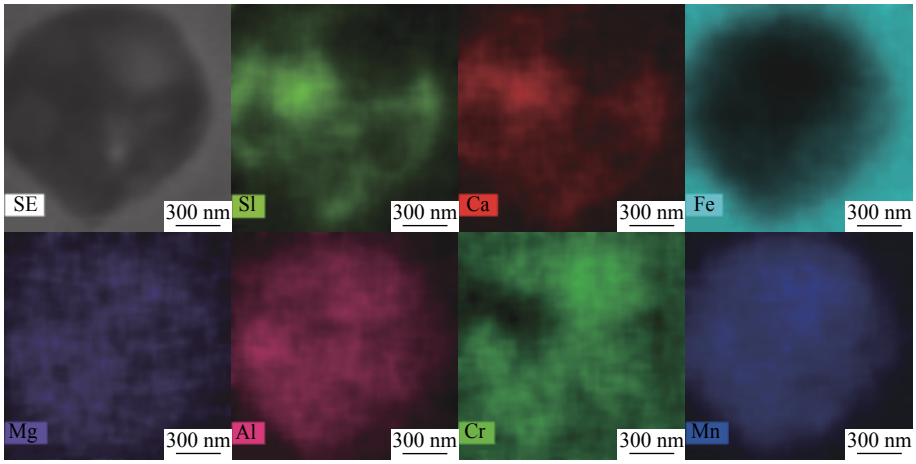

Fig. 9. SEM-mappings of typical inclusion in the steel after shocking for 60 min (3# sample).

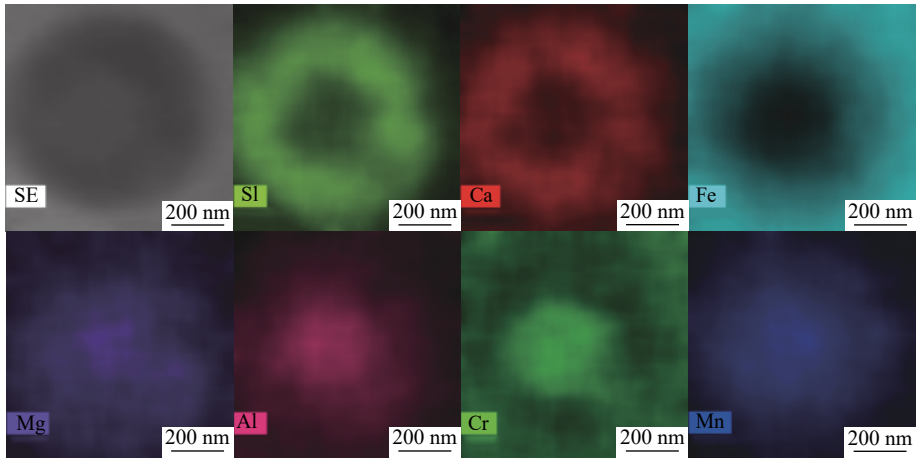

Fig. 10. SEM-mappings of typical inclusion in the steel after shocking for 120 min (4# sample).

perature rise, the inclusions grew gradually and austenite grain boundaries were observed. When the temperature rose to approximately 1100°C, high-temperature ferrites (σ) began to precipitate, as shown in Fig. 11(b). When the temperature was kept at 1250°C, the inclusion size further increased and high-temperature ferrite and austenite grain boundaries also grew further. During the soaking process at 1250°C, liquid phases surrounding the inclusions were observed, as shown in Fig. 11(d). The present CSLM observed results confirmed that MnO–SiO_2–Al_2O_3-based system inclusion existed in the

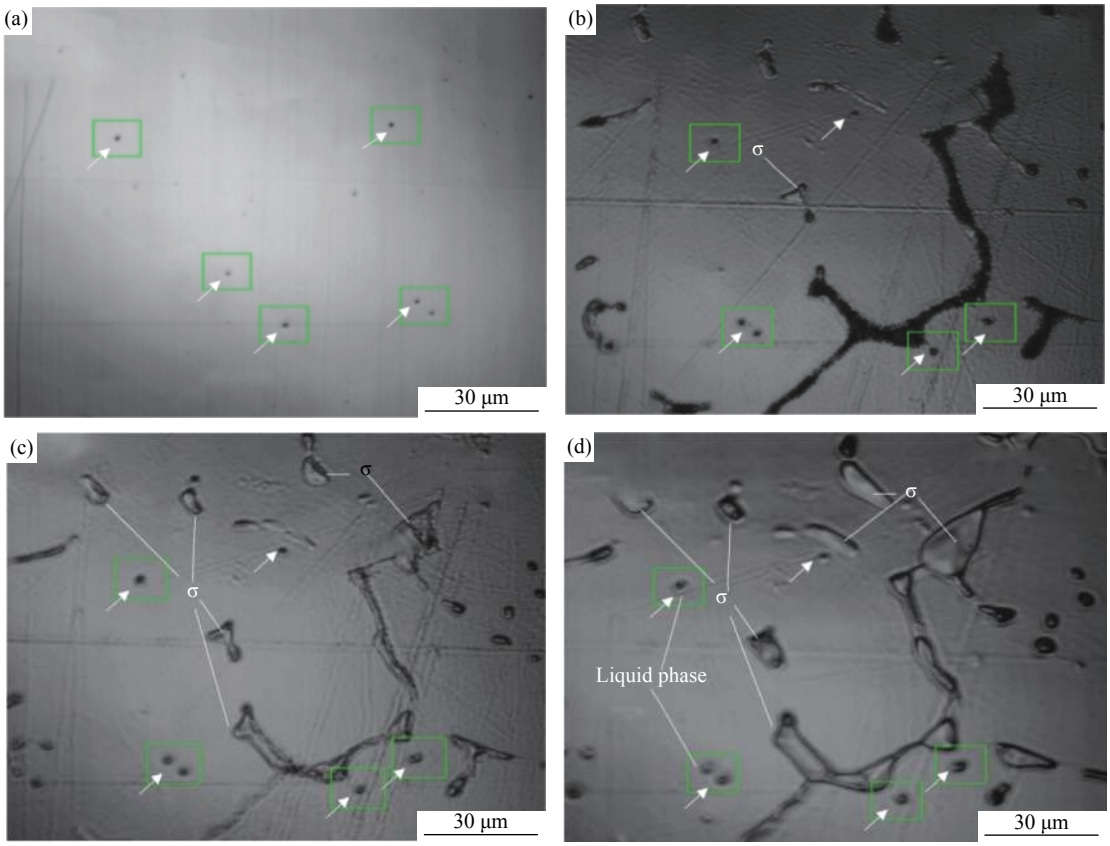

Fig. 11. ***In-situ*** **observation of the inclusion at different temperatures in the soaking process by CLSM: (a) 24.0°C; (b) 1100°C; (c) 1129°C; (d) 1250°C.**

liquid phase, or part of them existed in the liquid phase during soaking at 1250°C; thus, the interactions between the inclusion and steel matrix were much intense. In addition, some small inclusions disappeared with the other inclusion growth as well as the σ during the temperature rise and soaking process, which is the typical feature of Ostwald ripening.

3.5. Phase evolution and deformation of the inclusions after soaking process

Fig. 12 shows the variation of the liquid phase and $MnO–Cr_2O_3$ spinel phase in the inclusions of the steel samples with the different heat treatment time at 1250°C, calculated by FactSage 7.2 based on the average composition of inclusions shown in Fig. 4. With increasing heat treatment time, the $MnO–Cr_2O_3$ spinel phase in the inclusion increased correspondingly due to an increase in the Cr_2O_3 content. In addition, the amount of liquid phase in the inclusion declined sharply, suggesting that the plasticity of $MnO–SiO_2–Al_2O_3$-based inclusion would degenerate along with heat treatment due to the change in inclusion composition.

Fig. 13 and Table 2 show some typical inclusion morphologies and their composition observed in corresponding 0.3-mm thick cold-rolled strips subjected to soaking treatment at 1250°C for about 120 min before the rolling process. Inclusions (Nos. 1–3) are $MnO–Cr_2O_3–Al_2O_3$ inclusions with small sizes between 1 μm and 2 μm; those were almost not deformed during the rolling process. Inclusions (Nos. 4–9) are $MnO–SiO_2–Al_2O_3–Cr_2O_3$ based multi-component inclusions with different Cr_2O_3 content; some of the inclusions (Nos. 4–6) were rolled into string-like small particles, and some were deformed to different extents during rolling.

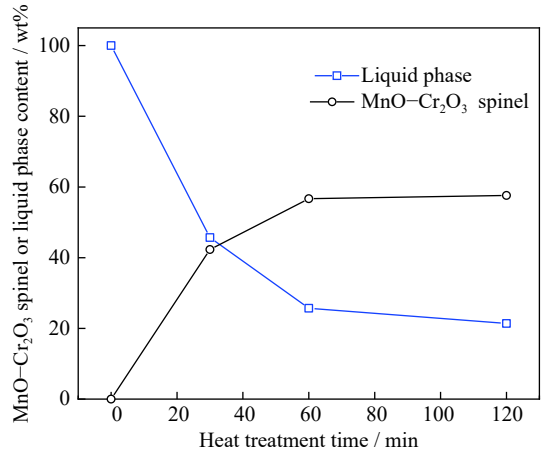

Fig. 12. Phase evolution of the inclusion with the different heat treatment time at 1250 °C, calculated by FactSage 7.2.

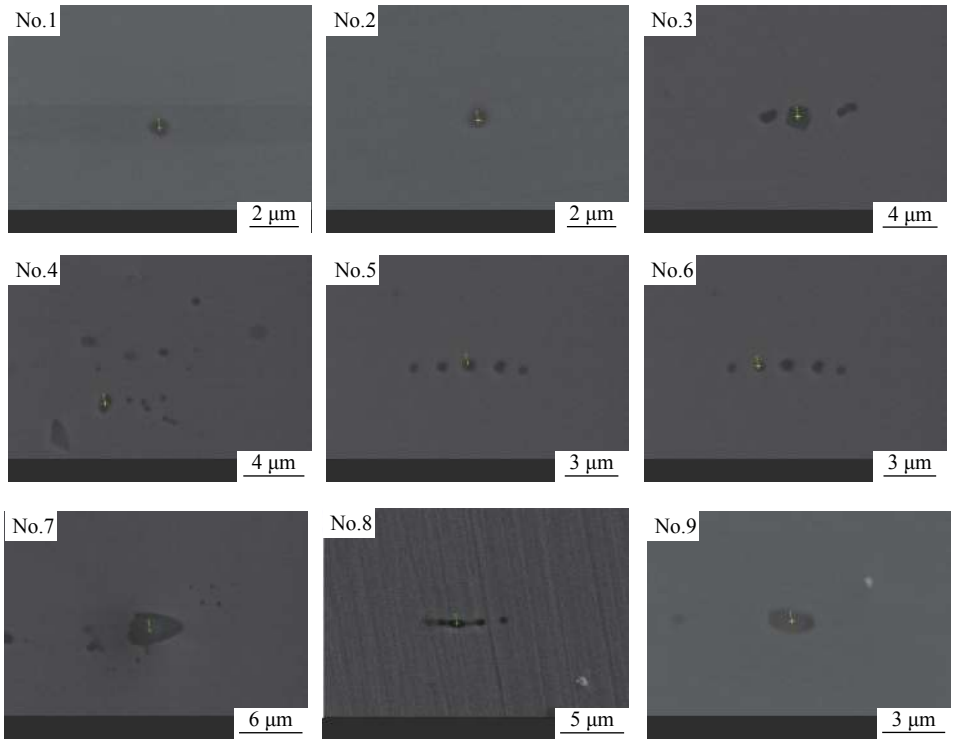

Fig. 13. Morphologies of some typical inclusions in corresponding cold-rolled strips.

Table 2. Composition and size of some typical inclusions in the cold-rolled strips as shown in the Fig. 13

No.	Composition / wt%						*d* / μm
	Al_2O_3	SiO_2	CaO	MgO	Cr_2O_3	MnO	
1	21.18	0.00	0.00	0.00	39.74	39.09	1.0
2	20.84	0.00	0.00	0.00	41.10	38.06	1.0
3	24.91	0.00	0.00	0.00	47.50	27.59	2.0
4	15.71	31.19	12.13	11.71	11.20	17.06	2.0
5	26.25	32.43	11.33	0.00	13.10	16.79	1.0
6	21.04	33.92	12.23	0.00	12.98	19.83	0.8
7	38.20	2.16	0.51	0.00	34.92	24.21	6.0
8	15.60	40.96	10.25	0.00	0.00	33.20	2.0
9	17.95	3.00	0.00	0.00	49.11	27.54	3.0

Note: *d* in the table means the inclusion equivalent diameter.

Some well-deformed inclusions, such as inclusion No.8, were also observed in the cold-rolled strips, and these were confirmed to be MnO–SiO_2–Al_2O_3-based inclusions with a very low or no Cr_2O_3 content. This verifies that the plasticity of inclusions deteriorated after the soaking process and the Cr_2O_3 content increased, which is consistent with the results in Fig. 12.

4. Discussion

4.1. Thermodynamic analysis

Fig. 14 shows the stable phase of the nonmetallic inclusion of 18wt%Cr–8wt%Ni stainless steel at 1250°C soaking temperature, calculated by FactSage 7.2, in which the tetragonal-spinel mainly consisted of MnO and Cr_2O_3 and a small amount of Al_2O_3. It can be seen that the $MnCr_2O_4$ spinel is the stable phase in equilibrium for 18wt%Cr–8wt%Ni stainless steel at 1250°C. This explains why MnO–Cr_2O_3-based inclusions precipitated during the soaking process. Some researchers [13,15] proposed that the formation of the $MnCr_2O_4$ spinel during the heat treatment process was due to the reaction between Cr in solid steel matrix and 2MnO–SiO_2-type inclusion, as shown in Eq. (1).

$$2[Cr] + 2MnO \cdot SiO_2 = MnO \cdot Cr_2O_3 + [Mn] + [Si] \quad (1)$$

The Cr in the steel matrix has the possibility of reacting with MnO, SiO_2 and Al_2O_3 in inclusions; thus, the thermodynamic analysis of these chemical reactions should be performed to better understand the inclusion evolution

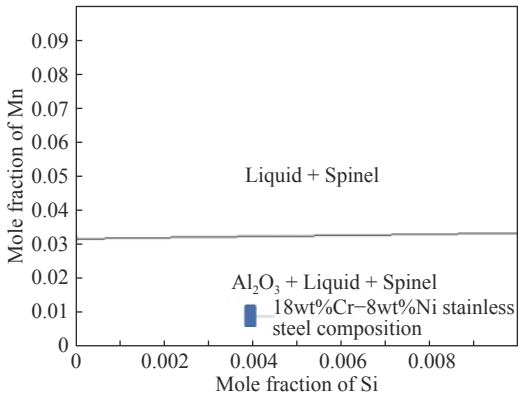

Fig. 14. Inclusion precipitate diagram of 18wt%Cr–8wt%Ni stainless steel with different Mn and Si contents at 1250°C, calculated by FactSage 7.2.

mechanism.

The reaction between Cr in the steel matrix [Cr] and MnO in inclusion (MnO), and its standard Gibbs energy $\Delta G_m^{\ominus}$ is expressed as Eqs. (2) and (3) [21]. Eq. (4) is the actual Gibbs free energy $\Delta G_{(MnO)}$ of the reaction (2).

$$2[Cr] + 3(MnO) = (Cr_2O_3) + 3[Mn] \quad (2)$$

$$\Delta G^{\ominus} = -84310 + 40.035T \quad (3)$$

$$\Delta G_{(MnO)} = \Delta G^{\ominus} + RT\ln\left(\frac{a_{[Mn]}^3 a_{(Cr_2O_3)}}{a_{[Cr]}^2 a_{(MnO)}}\right) \quad (4)$$

where R is gas constant, 8.314 J/(mol·K); T represents temperature, i.e., the soaking temperature, 1250°C in this study; and $a_{[Mn]}$ and $a_{[Cr]}$ are the element activities in the steel matrix relative to 1wt% standard state. Solid 18wt%Cr–8wt%Ni steel can be considered as a solid solution at the heat treatment temperature 1250°C; hence, in the present calculations, $a_{[Mn]}$ and $a_{[Cr]}$ are taken as mass percentages of Cr and Mn in steel, as well as $a_{[Si]}$, since activity coefficient could be taken as unity on the basis of the criterion of the component activity in a solid substance [22]. Moreover, $a_{(MnO)}$ and $a_{(Cr2O3)}$ indicate the MnO and Cr_2O_3 activities in the inclusion. Since at the soaking temperature, the Al_2O_3–SiO_2–MnO-based inclusions or most of them were in the liquid phase, the activities of the MnO and Cr_2O_3 were calculated by applying of the thermodynamic database F-oxide in the software FactSage 7.2 [23].

Similarly, the Gibbs free energies of the reactions between [Cr] and SiO_2, and between [Cr] and Al_2O_3 can be obtained according to their corresponding standard Gibbs free energies, as shown in Table 3. Table 4 shows the average content of the Al_2O_3–SiO_2–MnO-based inclusion and the corresponding activities calculated by FactSage 7.2 [23].

Fig. 15 shows the Gibbs free energy change of the three typical possible chemical reactions with different Cr_2O_3 contents in the inclusion at 1250°C. With increasing Cr_2O_3 content, the Gibbs free energy increased, indicating an increase in the difficulty of the occurrence of these chemical reactions. The Gibbs free energy for the reaction between Cr and MnO ($\Delta G_{(MnO)}$) is lower than 0 even when the inclusion has a large Cr_2O_3 content, and the Gibbs free energy between Cr and SiO_2 ($\Delta G_{(SiO_2)}$) is larger than 0 when the Cr_2O_3 content in the inclusion exceeded approximately 20wt%. For the reaction between Cr and Al_2O_3, the Gibbs free energy ($\Delta G_{(Al_2O_3)}$) is almost positive even when the inclusion has a very low Cr_2O_3 content. Hence, during the soaking process, the Cr is most likely to reduce the MnO in the inclusion, followed by the SiO_2, but not the Al_2O_3 content.

As shown in Figs. 4, 7–10, the MnO content in the inclusion was almost constant, which indicates that they were barely reduced, while SiO_2 and even CaO contents were reduced. This is not in agreement with the thermodynamic calculation results, as shown in Fig. 15. In addition, if MnO–Cr_2O_3-based inclusion is formed through the chemical

Table 3. Some possible reactions and their standard Gibbs free energy

Chemical reaction	Standard Gibbs free energy ($\Delta G_m^{\ominus}$) / (J·mol^{-1})	Reference
$2[Cr] + \frac{3}{2}(SiO_2) = Cr_2O_3 + \frac{3}{2}[Si]$	57350 + 30.525T	[21]
$2[Cr] + (Al_2O_3) = Cr_2O_3 + 2[Al]$	417690 − 35.975T	[21]

Table 4. Average composition and thier calculated activities of Al_2O_3–SiO_2–MnO inclusion at 1250 °C

Composition	Content / wt%	Activity a
Al_2O_3	16.9	0.057
SiO_2	39.5	0.28
MnO	43.6	0.21

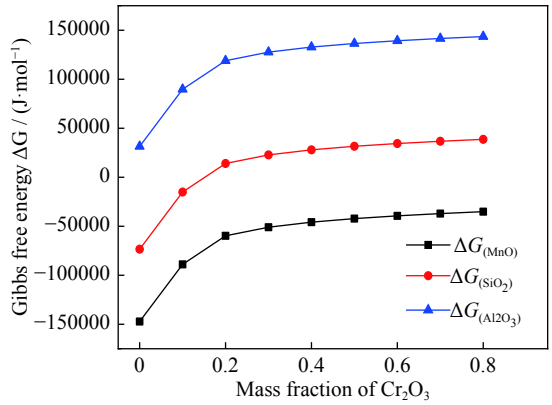

Fig. 15. Gibbs free energy change of the typical possible chemical reactions vs. Cr_2O_3 mass fraction in inclusions at 1250 °C soaking temperature.

reaction shown in Eq. (1), the inclusion size would be almost constant, but the inclusion diameter would significantly change in the present experimental results (shown as Fig. 5) as well as in the results of other studies [13,15]. In addition, according to the classical unreacted core model, the Cr should diffuse from the steel matrix to the inclusion, which means the Cr-enriched layer would expand from the outer layer to the inclusion center. However, some inclusions do not obey this law, as demonstrated in Figs. 8–10.

Therefore, there might be other methods to drive the inclusion evolution during soaking processes including chemical reactions.

4.2. Mechanism of inclusion evolution during soaking process

Ostwald ripening is a very common phenomenon for secondary-phase particle growth during heat treatment. According to the classical theory of Ostwald ripening [24], the interface energy is generated with the secondary-phase particle precipitation during the soaking process since a larger number of interfaces would be produced between the secondary-phase particle and the steel matrix. At a specific soaking temperature, the volume of the secondary-phase particle is determined by the solution product of the corresponding elements; thus, it is almost constant. Given the average inclusion radius r, the volume of a single inclusion particle is directly proportional to r^3; thus, the number of inclusions is negatively proportional to r^3, and the interface area between a single inclusion and the steel matrix is directly proportional to r^2. As a result, the total interface energy between all the inclusions and the steel matrix is negatively proportional to radius r, which indicates more interface energy within the steel would be generated when the inclusion has a smaller radius r. There is a chemical-free energy increment for an inclusion with a radius r relative to an inclusion with an infinite huge size, Δu, which is the driving force for Ostwald ripening, expressed as:

$$\Delta u = \frac{2\sigma V_p}{c_p r} \tag{5}$$

where σ is the specific interface energy, V_p represents the mole volume of the inclusion, and c_p is the mole fraction of the controlling element in equilibrium in the inclusion.

As a result, the driving force for Ostwald ripening is the interface energy, and it features the dissolution of the smaller inclusions and the growth of the larger inclusions due to them absorbing the smaller inclusions during the heat treatment. The present observations agree well with the features of Ostwald ripening, as shown in Fig. 5: the inclusions population density decreased and their average diameter increased during the soaking process. In addition, during the *in-situ* observation as in Fig. 11, inclusions grew following the disappearance of some small ones.

According to the inclusions observation experiment and the thermodynamic analysis, during the soaking process, inclusion evolution occurs in three routes: 1) many small-size $MnO–Cr_2O_3$ spinel particles precipitate and grow normally; 2) chemical reactions between Cr and $MnO–SiO_2–Al_2O_3$-based inclusion; 3) $MnO–SiO_2–Al_2O_3$-based inclusions and $MnO–Cr_2O_3$-based inclusions grow in the manner of Ostwald ripening by absorbing smaller $MnO–Cr_2O_3$ based particles.

Considering the second route, many researchers [13–15] have described the kinetic process based on an unreacted core model. Generally, there are three steps for this route: (1) Cr in the steel matrix and Mn^{2+} and Si^{4+} in the inclusion diffuse to the steel-inclusion interface; (2) the chemical reaction between [Cr] and the inclusion occurs at the steel-inclusion interface; (3) the product of the reaction (Cr^{3+}) diffuses from the interface to the inclusion matrix, and [Si] and [Mn] at the interface diffuse to the steel matrix. For this route, the diffusion of Cr in the steel matrix is usually considered as the controlling step [15].

The third route, the evolution process by Ostwald ripening, is described as follows, based on Reference [24].

(1) Many small faceted $MnCr_2O_4$ spinel inclusion precipitates surround the $MnO–SiO_2–Al_2O_3$-based inclusion or exist in the steel matrix.

(2) The small $MnCr_2O_4$ inclusions dissolve, and the Cr, Mn, and O diffuse to the surface of the $MnO–SiO_2–Al_2O_3$-based inclusion.

(3) The $MnCr_2O_4$ inclusions precipitate on the $MnO–SiO_2–Al_2O_3$-based inclusion again and diffuse to the other parts of the inclusion matrix to form Cr_2O_3-containing multi-component inclusions.

(4) Some $MnCr_2O_4$ inclusions would also grow by absorbing the neighboring smaller $MnCr_2O_4$ inclusions to form a larger $MnCr_2O_4$ spinel.

The controlling step for Ostwald ripening is much more complex to determine. According to the experimental results shown in Figs. 7–10 and 13, undissolved $MnO–Cr_2O_3$-concentrated regions were still observed within the inclusions after soaking for 120 min or in the final products; therefore, the dissolution of $MnO–Cr_2O_3$-based particles in $MnO–SiO_2–Al_2O_3$-based inclusion is deduced as the controlling step.

The above three routes always occur simultaneously during the soaking process; in particular, the latter two routes are

even likely to occur on the same inclusion. Thus, distinguishing which route is the dominant mechanism for $MnO–SiO_2–Al_2O_3$-based inclusion evolution during the soaking process is currently difficult, and hence, further investigation is needed. However, according to the experimental results and thermodynamic calculations, it can be concluded that Ostwald ripening plays a very important role in the $MnO–SiO_2–Al_2O_3$-based inclusion modification during the soaking process.

Furthermore, it should be pointed out that the $MnO–SiO_2–Al_2O_3$-based inclusion in a slab would crystallize during the heat treatment; CaO and SiO_2 would form some high-melting-point phases, such as wollastonite and melilite, which are in a solid state during the heat treatment, and other components such as MnO would form a liquid phase, as shown in Fig. 11. During stage (3) for inclusion evolution by Ostwald ripening during heat treatment, it is much easier for the $MnO–Cr_2O_3$ based particles to dissolve in the low-melting phase and much difficult to diffuse to the solid phases, which are mainly composed of CaO and SiO_2. As a result, the $MnO–Cr_2O_3$-enriched region and the $CaO–SiO_2$-concentrated region within the inclusions after soaking usually seem incompatible and complementary, as shown in Figs. 8–10.

5. Conclusions

The evolution of $MnO–Al_2O_3–SiO_2$-based inclusion of 18wt%Cr–8wt%Ni stainless steel under isothermal soaking process at 1250°C was investigated by laboratory-scale experiments. The following conclusions are obtained.

Firstly, during the soaking process, the inclusion population density increased at the first stage and then decreased, and their average size first decreased and then increased due to a large number of $MnO–Cr_2O_3$ particles precipitating and their subsequent growth.

Secondly, there are almost no Cr_2O_3-concentrated regions before soaking, but more and more Cr_2O_3-enriched region precipitated as the soaking proceeded. Correspondingly, the high-melting-point $MnO–Cr_2O_3$ spinel phase in the inclusion increased, and the amount of liquid phase in the inclusion declined sharply, resulting in the degeneration in the plasticity of $MnO–SiO_2–Al_2O_3$-based inclusion along with heat treatment.

Thirdly, high-temperature CLSM observations confirmed the production of liquid phases, and these phases accelerated the inclusion growth process.

Finally, both the experimental results and thermodynamic analysis show that there are three routes for inclusion evolution during the soaking process: 1) many small-size $MnO–Cr_2O_3$ spinel particles precipitate and grow; 2) chemical reactions between Cr and $MnO–SiO_2–Al_2O_3$-based inclusion; 3) Ostwald ripening, i.e. the $MnO–SiO_2–Al_2O_3$-based inclusions and $MnO–Cr_2O_3$-based inclusions grow by absorbing smaller $MnO–Cr_2O_3$-based particles. Ostwald ripening plays an important role in the inclusion evolution during the soaking process.

Acknowledgements

The work was financially supported by the National Science Foundation for Young Scientists of China (No. 5170402), the China Postdoctoral Fund (No. 2018M630071), the Fundamental Research Funds for the Central Universities (No. RF-TP-19-030A2), and the Joint Funds of the National Natural Science Foundation of China (No. U1560203).

References

[1] J.H. Park and H. Todroki, Control of $MgAl_2O_4$ spinel inclusions in stainless steels, *ISIJ Int.*, 50(2010), No. 10, p. 1333.

[2] J.H. Park and Y. Kang, Inclusions in stainless steels—A review, *Steel Res. Int.*, 88(2017), No. 12, art. No. 1700130.

[3] H. Suito and R. Inoue, Thermodynamics on control of inclusions composition in ultra-clean steels, *ISIJ Int.*, 36(1996), No. 5, p. 528.

[4] Z.L. Xue, Z.B. Li, J.W. Zhang, W. Yang, C.F. Gan, and Y. Wang, Theory and practice of oxide inclusion composition and morphology control in spring steel production, *J. Iron Steel Res. Int.*, 10(2003), No. 2, p. 38.

[5] L.F. Zhang and B.G. Thomas, State of the art in evaluation and control of steel cleanliness, *ISIJ Int.*, 43(2003), No. 3, p. 271.

[6] G. Benard, P.V. Ribound, and G. Urbain, Oxide inclusions plasticity, *Rev. Met. Paris*, 78(1981), No. 5, p. 421.

[7] Y.B. Kang and H.G. Lee, Inclusions chemistry for Mn/Si deoxidized steels: thermodynamic predictions and experimental confirmations, *ISIJ Int.*, 44(2004), No. 6, p. 1006.

[8] Y. Ren, L.F. Zhang, W. Fang, S.J. Shao, J. Yang, and W.D. Mao, Effect of slag composition on inclusions in Si-deoxidized 18Cr–8Ni stainless steels, *Metall. Mater. Trans. B*, 47(2016), No. 2, p. 1024.

[9] C. Gu, Y.P. Bao, P. Gan, M. Wang, and J.S. He, Effect of main inclusions on crack initiation in bearing steel in the very high cycle fatigue regime, *Int. J. Miner, Metall. Mater.*, 25(2018), No. 6, p. 623.

[10] Q.K. Yang, P. Shen, D. Zhang, Y.X. Wu, and J.X. Fu, Analysis on composition and inclusions of ballpoint pen tip steel, *Int. J. Miner, Metall. Mater*, 25(2018), No. 4, p. 420.

[11] K. Takano, R. Nakao, S. Fukumoto, T. Tsuchiyama, and S. Takaki, Grain size control by oxide dispersion in austenitic stainless steel, *Tetsu-to-Hagane*, 89(2003), No. 5, p. 616.

[12] H. Shibata, T. Tanaka, K. Kimura, and S.Y. Kitamura, Composition change in oxide inclusions of stainless steel by heat treatment, *Ironmaking Steelmaking*, 37(2010), No. 7, p. 522.

[13] H. Shibata. K. Kimura. T. Tanaka, and S. Kitamura, Mechanism of change in chemical composition of oxide inclusions in Fe–Cr Alloys deoxidized with Mn and Si by heat treatment at 1473 K, *ISIJ Int.*, 51(2011), No. 12, p. 1944.

[14] T. Taniguchi, N. Satoh, Y. Saito, K. Kubota, A. Kumagai, Y. Tamura, and T. Miki, Investigation of compositional change of inclusions in martensitic stainless steel during heat treatment by newly developed analysis method, *ISIJ Int.*, 51(2011), No. 12, p. 1957.

[15] Y. Ren, L.F. Zhang, and P.C. Pistorius, Transformation of oxide inclusions in type 304 stainless steels during heat treatment, *Metall. Mater. Trans. B*, 48(2017), No. 5, p. 2281.

[16] J.J. Wang, W.F. Li, Y. Ren, and L.F. Zhang, Thermodynamic and kinetic analysis for transformation of oxide inclusions in solid 304 stainless steels, *Steel Res. Int.*, 90(2019), No. 7, art. No. 1800600.

[17] X.F. Bai, Y.H. Sun, R.M. Chen, Y.M. Zhang, and Y.F. Cai, Formation and thermodynamics of CaS-bearing inclusions during Ca treatment in oil casting steels, *Int. J. Miner. Metall. Mater.*, 26(2019), No. 5, p. 573.

[18] C.S. Liu, S.F. Yang, K.H. Kim, J.S. Li, H. Shibata, and S.Y. Kitamura, Influence of FeO and sulfur on solid state reaction between MnO−SiO_2−FeO oxides and an Fe−Mn−Si solid alloy during heat treatment at 1473 K, *Int. J. Miner. Metall. Mater.*, 22(2015), No. 8, p. 811.

[19] Y.P. Chu, W.F. Li, Y. Ren, and L.F. Zhang, Transformation of inclusions in linepipe steels during heat treatment, *Metall. Mater. Trans. B*, 50(2019), No. 4, p. 2047.

[20] X.X. Luo, H.T. Zhang, X. Han, S.J. Guo, D.D. Chen, J.Z. Cui, and H. Nagaumi, Development of inclusions in 3104 alloy melt during heating and holding treatments, *Int. J. Miner. Metall. Mater.*, 23(2016), No. 6, p. 637.

[21] *Steelmaking Data Sourcebook*, The Japan Society for the Promotion of Science: The 19th Committee on Steelmaking ed., Gordon and Breach Science Publishers, Tokyo, 1988.

[22] H.J. Guo. *Physical Chemistry of Metallurgy*, 2nd, Metallurgical Industry Press, Beijing, 2006, p. 6.

[23] I.H. Jung, S.A. Decterov, and A.D. Pelton, Computer applications of thermodynamic databases to inclusion engineering, *ISIJ Int.*, 44(2004), No. 3, p. 527.

[24] I.M. Lifshitz and V.V. Slyozov, The kinetics of precipitation from supersaturated solid solutions, *J. Phys. Chem. Solids*, 19(1961), No. 1-2, p. 35.